Assimilation of Synthetic GOES-R ABI Infrared Brightness Temperatures and WSR-88D Radar Observations in a High-Resolution OSSE

REBECCA M. CINTINEO AND JASON A. OTKIN

Cooperative Institute for Meteorological Satellite Studies, University of Wisconsin–Madison, Madison, Wisconsin

THOMAS A. JONES

Cooperative Institute for Mesoscale Meteorological Studies, University of Oklahoma, and NOAA/OAR/National Severe Storms Laboratory, Norman, Oklahoma

STEVEN KOCH

NOAA/OAR/National Severe Storms Laboratory, Norman, Oklahoma

DAVID J. STENSRUD

Department of Meteorology, The Pennsylvania State University, University Park, Pennsylvania

ABSTRACT

This study uses an observing system simulation experiment to explore the impact of assimilating GOES-R Advanced Baseline Imager (ABI) 6.95-μm brightness temperatures and Weather Surveillance Radar-1988 Doppler (WSR-88D) reflectivity and radial velocity observations in an ensemble data assimilation system. A high-resolution truth simulation was used to create synthetic radar and satellite observations of a severe weather event that occurred across the U.S. central plains on 4–5 June 2005. The experiment employs the Weather Research and Forecasting Model at 4-km horizontal grid spacing and the ensemble adjustment Kalman filter algorithm in the Data Assimilation Research Testbed system. The ability of GOES-R ABI brightness temperatures to improve the analysis and forecast accuracy when assimilated separately or simultaneously with Doppler radar reflectivity and radial velocity observations was assessed, along with the use of bias correction and different covariance localization radii for the brightness temperatures. Results show that the radar observations accurately capture the structure of a portion of the storm complex by the end of the assimilation period, but that more of the storms and atmospheric features are reproduced and the accuracy of the ensuing forecast improved when the brightness temperatures are also assimilated.

1. Introduction

The high temporal and spatial resolution of three-dimensional radar observations and their ability to provide information about atmospheric motion and cloud hydrometeors make them useful observations to assimilate into numerical weather prediction (NWP) models. Many studies have investigated the impact of assimilating radar observations in high-resolution numerical models using ensemble-based (e.g., Snyder and Zhang 2003; Dowell et al. 2004; Tong and Xue 2005; Dawson et al. 2012; Jung et al. 2012; Yussouf et al. 2013; Kerr et al. 2015) and variational methods (e.g., Sun and Crook 1997, 1998; Sun and Crook 2001; Xiao et al. 2005; Hu et al. 2006a,b; Schenkman et al. 2011; Gao and Stensrud 2012). They have been shown to improve atmospheric analyses and lead to more accurate short-range forecasts. Unlike surface-based radars, satellite sensors can provide information about the atmospheric state in both clear and cloudy areas over the entire globe. Polar-orbiting satellites provide observations with high spatial and spectral resolution but are limited

Corresponding author address: Jason Otkin, CIMSS, University of Wisconsin–Madison, 1225 West Dayton St., Madison, WI 53706. E-mail: jasono@ssec.wisc.edu

to only two overpasses each day over a given location. Geostationary satellite sensors often have lower spectral resolution than polar orbiters but observe a given location with much greater frequency. This allows them to provide information on features that evolve over short time scales and are thus useful for regional-scale modeling systems that assimilate observations with high temporal frequency (e.g., hourly or less).

The current version of the Geostationary Operational Environmental Satellite (GOES) imagers provide observations approximately every 15 min over the continental United States (CONUS) in five spectral bands with nadir horizontal resolutions of 1 km for the visible band and 4 km for the infrared bands. Observations with higher temporal, spectral, and spatial resolution will be available with the expected launch of the GOES-R Advanced Baseline Imager (ABI) sensor in 2016. With the launch of ABI, observations will be available over CONUS at 5-min intervals for 16 spectral bands and with finer spatial resolution, including an increase to 2 km for the infrared bands (Schmit et al. 2005). In preparation for using ABI observations and to assess their impact on model forecasts, an observing system simulation experiment (OSSE) is performed in this study to explore their potential impact in a high-resolution ensemble data assimilation system when assimilated alone or in combination with Weather Surveillance Radar-1988 Doppler (WSR-88D) reflectivity and radial velocity observations.

Despite their advantages of having high spatial and temporal resolution, the assimilation of geostationary satellite observations in NWP systems has not been investigated as extensively as many other observation types. Several studies have explored the assimilation of geostationary satellite data in global and limited area models. Vukicevic et al. (2004) assimilated visible and 10.7-μm infrared window *GOES-9* radiances in a four-dimensional variational data assimilation (4DVAR) system for a case characterized by low-level stratus cloud. There was a positive impact on the cloud field in the analysis and short-term forecast, but less improvement in the clear-sky areas because the satellite observations had little sensitivity there. Vukicevic et al. (2006) used 4DVAR to assimilate the 10.7- and 12.0-μm infrared radiances from GOES for a multilevel nonprecipitating cloud case. Upper-level ice clouds were improved, but not liquid clouds when they occurred below thick ice clouds. Additional improvements also occurred when using more channels or with more frequent assimilation cycles. Stengel (2008) and Stengel et al. (2009, 2013) also used 4DVAR to assimilate infrared radiances from the Spinning Enhanced Visible and Infrared Imager (SEVIRI) sensor into a high-resolution

model. They investigated the assimilation of clear and cloudy observations for the 6.2- and 7.3-μm water vapor channels and the 13.4-μm CO_2 channel for 1- and 2-month periods and found the observations contributed to more accurate analyses and forecasts, especially when including cloud-affected radiances. Privé et al. (2013) explored the impact of a wide variety of both polar-orbiting and geostationary satellite radiances using a 3DVAR data assimilation system. The geostationary radiances had a positive impact on analyzed global geopotential heights, though less than the polar orbiter radiances.

Ensemble data assimilation systems have been used to explore the potential impact of assimilating ABI infrared brightness temperatures. Otkin (2010) used an ensemble adjustment Kalman filter (EAKF) to assimilate clear and cloudy 8.5-μm infrared brightness temperatures for a large extratropical cyclone during the same 4–5 June 2005 time period explored in this study. The current study, however, uses smaller horizontal grid spacing and assimilates both radar and satellite observations at a much higher temporal frequency. Otkin (2010) showed that brightness temperature assimilation improved the cloud field, particularly when both clear and cloudy observations were assimilated. Zupanski et al. (2011) evaluated the ability of ABI 10.35-μm infrared window observations to reduce cloud location errors when assimilated using the maximum likelihood ensemble filter (MLEF). Jones et al. (2013b) also used an EAKF to assimilate ABI 6.95-μm infrared water-vapor-sensitive brightness temperatures, in addition to WSR-88D reflectivity and radial velocity, for a cool season extratropical cyclone. They found that the radar observations had the largest impact on the wind and cloud analyses in the lower troposphere and that the infrared brightness temperatures afforded additional improvements in the water vapor and cloud analyses in the mid- and upper troposphere. Jones et al. (2014) continued that study by evaluating subsequent 1–3-h forecasts and found that assimilating ABI 6.95-μm brightness temperatures produced more accurate water vapor and ice cloud forecasts, whereas the radar reflectivity and radial velocity observations improved the low-level cloud distribution. Their results also showed that the best analysis and forecast occurred when assimilating both observation types.

Other recent studies have investigated the assimilation of derived cloud variables instead of the direct assimilation of the satellite radiances. Jones et al. (2013a, 2015) and Jones and Stensrud (2015) assimilated cloud water path (CWP) retrievals in an EAKF system for a severe weather event and found that storms spin up faster when CWP and radar observations are assimilated

simultaneously. Kerr et al. (2015) used an EAKF in an OSSE to assimilate synthetic ABI cloud-top temperature and WSR-88D observations for an idealized supercell thunderstorm. Though their results showed that the cloud-top temperature retrievals were not as valuable as radar observations, they were able to create supercell storms in regions where no radar data were available. Together, these studies have shown the benefits of assimilating cloud retrievals, despite the introduction of additional uncertainty in the observations originating from the retrieval algorithm.

Most early infrared satellite assimilation studies focused on clear-sky observations since observations in cloudy or precipitating regions are more difficult to assimilate because of their nonlinear and discontinuous nature and the shorter predictability of cloud features (e.g., Errico et al. 2007; Fabry and Sun 2010; Bauer et al. 2011). However, the importance of assimilating cloudy radiances has been demonstrated in several studies during the past decade (e.g., Andersson et al. 2005; Errico et al. 2007; Vukicevic et al. 2004, 2006; Stengel et al. 2009, 2013; Otkin 2010; 2012a,b; Privé et al. 2013). Smaller model grid spacing is used in this study compared to these prior studies, most of which employed resolutions that were 10 km or larger. More recent studies that assimilated derived cloud variables used finer model grid spacing closer to the 4-km grid spacing used in this study. Jones et al. (2015) assimilated *GOES-13* CWP and WSR-88D reflectivity and radial velocity into a 3-km model while Jones and Stensrud (2015) used a 2-km idealized model for assimilating synthetic *GOES-13* CWP using multiple cloud microphysics schemes. However, those studies did not assimilate the brightness temperatures directly as is done in this study.

Section 2 describes the truth simulation used for the OSSE and the synthetic observations created from that simulation are described in section 3. The assimilation experiment setup is described in section 4. Sections 5 and 6 examine the use of bias correction and different horizontal localizations in the assimilation of the brightness temperatures, and section 7 shows the relative impacts of assimilating the brightness temperatures and radar observations both separately and together. Finally, section 8 provides a summary and discussion of the results.

2. Truth simulation

The severe weather event simulated in this OSSE occurred over the central United States on 4 June 2005. A strong shortwave trough, deep layer shear, and high instability due to the advection of abundant lower tropospheric moisture and strong surface heating led the

Storm Prediction Center (SPC) to issue a high risk for severe weather outlook across the region. A Particularly Dangerous Situation tornado watch was subsequently issued for parts of Kansas, Nebraska, Iowa, and Missouri ahead of a dryline extending across central Kansas and to the south of a warm front extending northeastward into Minnesota and Wisconsin (Storm Prediction Center 2015).

A 2-km horizontal resolution "truth" simulation of the event (hereafter TRUTH) was performed using version 3.4.1 of the Advanced Research Weather Research and Forecasting (WRF) Model (ARW; Skamarock et al. 2008) initialized using North American Mesoscale Forecast System (NAM) analyses. The simulation contained a 400×400 gridpoint domain with 53 vertical levels and a model top of 50 hPa. It employed the WRF single-moment 6-class (WSM6) microphysics scheme (Hong et al. 2004; Hong and Lim 2006), Dudhia longwave and shortwave radiation schemes (Dudhia 1989; Chen and Dudhia 2001), Yonsei University (YSU) planetary boundary layer scheme (Hong et al. 2006), and the Noah land surface model. The TRUTH simulation was initialized at 2100 UTC 4 June 2005, just prior to convective initiation in the region of interest, and then integrated for a 3-h period with output files generated at 5-min intervals.

3. Simulated observations

a. Doppler radar observations

Synthetic radar reflectivity and radial velocity observations were created using data from the TRUTH simulation for three WSR-88Ds (Wichita, Kansas; Topeka, Kansas; and Kansas City, Missouri) that provided good coverage of the thunderstorms (Fig. 1). Observations from surrounding radars were not generated to reduce computational expense during the assimilation experiments. The synthetic radar observations were generated for each radar by first creating a set of observation locations based on the volume coverage pattern 21 (VCP 21) scanning strategy containing nine elevation angles from 0.5° to 19°, with 4-km range bins at an azimuthal spacing of 3.0° to a maximum range of 200 km. Simulated radar observations were then generated on the model grid points using the in-code WRF reflectivity calculations specific to the WSM6 microphysics scheme and then interpolated to the radar observation locations. Random errors were not added to the observations. Radar reflectivity observations <10 dBZ were not assimilated during the experiments and radial velocities were only assimilated where the reflectivity was >0 dBZ. Though clear-air reflectivity observations were not assimilated, it is important to note that they do not necessarily
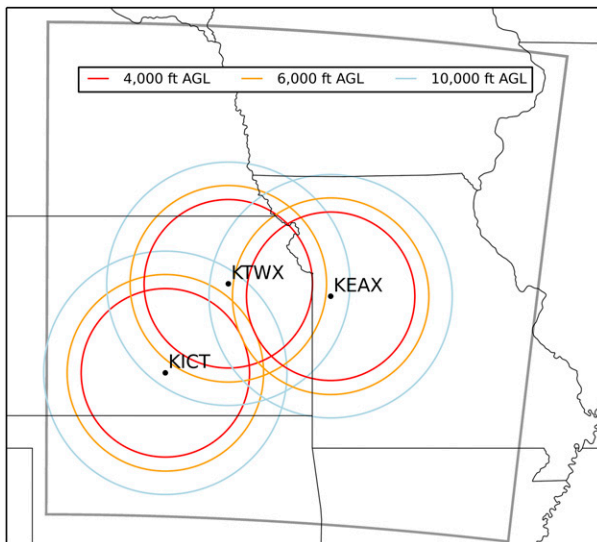
FIG. 1. Model domain for the TRUTH simulation and data assimilation experiments. The locations and ranges of the simulated WSR-88Ds are also shown.

indicate cloud-free conditions and have been shown to be ineffective at removing anomalous nonprecipitating clouds from the model analysis (Jones et al. 2016). The observation error standard deviations for the radar reflectivity and radial velocity observations are set to 5 dBZ and 2 m s^{-1}, respectively, which are similar to previous studies (e.g., Aksoy et al. 2009; Yussouf et al. 2013).

b. GOES-R ABI band 9 (6.95 μm) brightness temperatures

Band 9 on the ABI sensor is an infrared water-vapor-sensitive channel with a central wavelength of 6.95 μm that provides information about clouds and water vapor in the middle and upper troposphere. Synthetic 6.95-μm brightness temperatures were created from the TRUTH simulation using the Successive Order of Interaction (SOI) forward radiative transfer model (Heidinger et al. 2006; O'Dell et al. 2006). Both the creation and assimilation of the synthetic brightness temperatures use the Seemann et al. (2008) surface emissivity dataset. The satellite observations were averaged from their original 2-km resolution to a spatial resolution of 6 km prior to their assimilation. Only observations that were completely clear or completely cloudy (as identified using cloud hydrometeor mixing ratios from the TRUTH simulation) within the averaging interval were used during the assimilation experiments. An observation error of 3.3 K is used for both clear- and cloudy-sky observations, similar to Otkin (2012b). The use of a constant observation error has proven effective in prior studies; however, future studies will explore the use of

cloud-dependent observation error models similar to those developed by Geer and Bauer (2011), Okamoto et al. (2014), and Harnisch et al. (2016).

c. Conventional observations

Conventional radiosonde and surface observations were created every 6 h from 0000 UTC 2 June to 1200 UTC 5 June 2005. The radiosonde observations are vertical profiles of wind, temperature, and water vapor mixing ratio up to 50 hPa at upper-air observation locations. Synthetic surface observations created for Automated Surface Observing System (ASOS) locations include the surface pressure, 10-m wind speed and direction, and 2-m temperature and water vapor mixing ratio. Measurement errors for each observation type were drawn from an uncorrelated Gaussian random distribution of error values typical for the sensor.

4. WRF Model and ensemble data assimilation configuration

The assimilation experiments also use version 3.4.1 of the ARW model and the same domain as TRUTH, except for using 4-km horizontal grid spacing and a 10-hPa model top. The clear-sky weighting function profile for the 6.95-μm channel is mostly below 50 hPa, so the majority of the signal comes from below the model tops in both the TRUTH and data assimilation experiments. The EAKF algorithm in the Data Assimilation Research Testbed (DART) system (Anderson 2001) is employed for the assimilation experiments using 50 ensemble members for all experiments. The ensemble members are generated following the method described by Torn et al. (2006). The National Meteorological Center (NMC, now known as NCEP) method (Parrish and Derber 1992) is used in the WRF-Var system to generate background error covariances from five 24- and 48-h forecasts begun at 0000 UTC on 1–5 June 2005. An initial Global Forecast System (GFS) analysis file is then perturbed with those background errors to create an ensemble of initial and lateral boundary conditions.

The Noah land surface model and the YSU planetary boundary layer scheme are used for the experiments. While the TRUTH simulation uses the NAM model for initial and boundary conditions, the experiments use the perturbed GFS analyses. The temporally and spatially varying adaptive covariance inflation method described by Anderson (2007, 2009) is applied to the prior ensemble at each assimilation time to help maintain ensemble spread. Whereas the SOI forward radiative transfer model was used to compute the synthetic satellite observations from the TRUTH simulation, the Community Radiative Transfer Model (CRTM; Han

et al. 2006) was used to compute the model equivalent brightness temperatures during the assimilation experiments. Other differences between TRUTH and the experiments are the choice of cloud microphysics and radiation schemes. While TRUTH employs WSM6, the experiments use the Thompson microphysics scheme (Thompson et al. 2004, 2008). No convective parameterization scheme was used for any of the simulations. The experiments use the Rapid Radiative Transfer Model for General Circulation Models (RRTMG) longwave and shortwave radiation schemes (Iacono et al. 2008). The different model resolutions, initialization datasets, forward radiative transfer models, microphysics, and radiation schemes used in TRUTH and the assimilation experiments eliminates the possibility of performing "identical twin" experiments characterized by insufficient model error, which can bias conclusions about data impact (Atlas et al. 1985). However, they also introduce differences in the model environment that can complicate interpretations of the experiment results.

The 50-member ensemble is initialized at 0000 UTC on 2 June 2005 and allowed to freely evolve for 24 h in order to increase the ensemble spread before synthetic radiosonde and surface observations created from the NAM analyses are assimilated every 6 h during an additional 45-h spinup period. The experiments then assimilate the synthetic satellite and radar observations every 5 min for a 2-h assimilation period from 2100 until 2300 UTC 4 June, at which time a 1-h ensemble forecast is begun. Gaspari and Cohn (1999) covariance localization is used in this study. The radar reflectivity and radial velocity observations use horizontal and vertical half-width localizations of 4 km, whereas the brightness temperatures use a horizontal localization half-width of 28 km and no vertical localization, given that they are sensitive to a broad layer of the atmosphere. Horizontal localization for the brightness temperatures is discussed further in section 6.

5. Brightness temperature bias correction

Several sources can introduce bias in an assimilation system, including the observations, the radiative transfer model, the NWP model, and initial and lateral boundary conditions. Previous studies have investigated relatively complicated bias correction schemes when assimilating clear-sky satellite radiances, including the use of airmass-dependent model predictors and accounting for variations in geography and time (e.g., Harris and Kelly 2001). The present study uses a simple fixed-value bias correction, similar to that used in Stengel (2008) and Stengel et al. (2009, 2013). Given the short duration of this OSSE, the simulated clear-sky observations were bias corrected using the average bias in the
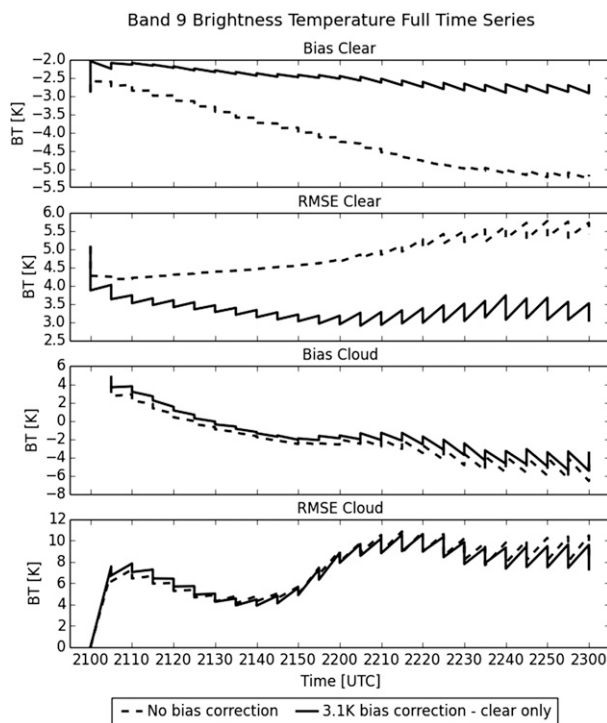

FIG. 2. ABI band 9 (6.95 μm) brightness temperature (K) bias and root-mean-square error (RMSE) time series during the assimilation period for satellite assimilation experiments with (solid line) and without (dashed line) bias correction.

clear-sky regions (3.1 K) at the start of the assimilation period. Bias correction was not applied to the cloudy observations because their bias error characteristics varied greatly with time because of changes in the cloud field. This provides evidence that more sophisticated bias correction methods based on observed cloud properties such as cloud-top height may be necessary to effectively remove the bias from cloud-affected observations.

Figure 2 shows the evolution of the bias and RMSE during the assimilation period computed with respect to the clear and cloudy grid points in the TRUTH simulation. A grid point was considered cloudy if it had a total CWP greater than zero. The domain-averaged statistics shown here and in the rest of the paper exclude 20 grid points from the domain edges to reduce the impact of the lateral boundaries. The largest reduction in the cold bias occurs during the initial assimilation cycle. The bias increases each time the model advances to the next assimilation cycle, but is reduced again when new observations are assimilated. The bias correction reduces the clear-sky bias to −2.7 K by the end of the assimilation period as compared to −5.1 K without the bias correction (Fig. 2). It also reduces the final analysis RMSE from 5.3 to 3 K. The use of a bias correction for
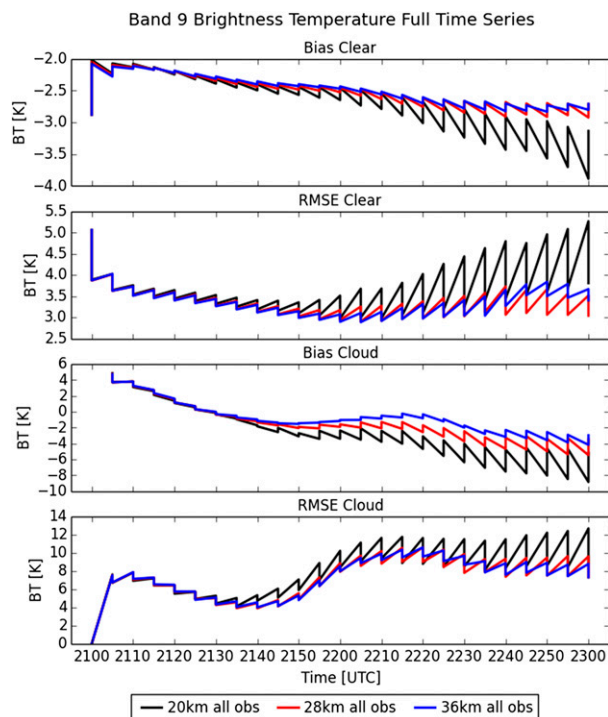
Band 9 Brightness Temperature Full Time Series

FIG. 3. ABI band 9 (6.95 μm) brightness temperature (K) bias and RMSE time series during the assimilation period for satellite assimilation experiments using a 20- (black), 28- (red), or 36-km (blue) horizontal localization radius for the brightness temperature observations. The top two panels show the statistics where the TRUTH simulation is cloud-free, whereas the bottom two panels show the statistics where the TRUTH simulation has clouds.

the clear-sky observations also led to a slight improvement in the cloudy statistics.

6. Brightness temperature horizontal localization

Covariance localization is the maximum distance at which a given observation is allowed to impact a state variable. It allows for a relatively small ensemble to be used in ensemble assimilation systems by helping account for the small ensemble size relative to the degrees of freedom in the model state vector (e.g., Houtekamer and Mitchell 2001, Whitaker and Hamill 2002, Ott et al. 2004).

Figure 3 shows the time series of the domain-averaged bias and RMSE computed with respect to the clear and cloudy grid points in the TRUTH simulation during the 2-h assimilation period when using different horizontal localization radii for the ABI 6.95-μm observations. Overall, the bias and RMSE were smallest for clear-sky grid points when the 28-km radius was used, with larger errors occurring when the 20- and 36-km radii were used. The errors were larger when using the 20-km radius because the observations were unable to effectively remove erroneous clouds from clear areas of the domain

given the shorter radius of influence. A larger 36-km radius promoted the removal of the excess cloud cover; however, the RMSE was still higher than the 28-km case because spurious thunderstorms were introduced in areas to the north of the main convective line (not shown). The 28-km radius was able to remove the excess clouds in clear-sky areas without creating the extra thunderstorms and thus had the lowest bias and RMSE. For cloudy grid points, the 28- and 36-km radii produced the smallest RMSE and bias, whereas the 20-km radius was again characterized by the largest errors. Thus, based on these results, the localization radius was set to 28 km for both clear- and cloudy-sky observations during the assimilation experiments described in the next section. This localization radius is smaller than that used in prior studies by Otkin (2012b) and Jones et al. (2013b); however, it is a reasonable value considering the higher horizontal resolution used in the current study. A shorter radius is necessary to account for the finescale cloud and water vapor features in the simulated satellite observations.

7. Radar and satellite assimilation experiments

a. Observation space diagnostics

The impact of assimilating WSR-88D radar reflectivity and radial velocity observations and ABI 6.95-μm brightness temperatures, both separately and combined, is investigated using a control experiment in which no observations are assimilated (CTRL) and experiments in which only satellite (SAT), only radar (RAD), or both satellite and radar (SATRAD) observations are assimilated. The root-mean-square innovation (RMSI) and ensemble spread are observation space diagnostics computed for the brightness temperature, radar reflectivity, and radial velocity observations at each assimilation cycle for the SAT, RAD, and SATRAD experiments. The RMSI gives the fit of the observations to the model state before and after the assimilation and is defined as

$$ \text{RMSI} = \sqrt{\frac{1}{N}\sum_{n=0}^{N}[y_n - H(x_n)]^2}, \qquad (1) $$

where y is the observation, $H(x)$ is the prior or posterior model state, and N is the total number of observations. The expression within the square brackets is the innovation. The total ensemble spread is a combination of the observation error and ensemble spread:

$$ \text{Total Spread} = \sqrt{\sigma_{\text{obs}}^2 + \left\langle \frac{1}{E-1}\sum_{e=0}^{E}[H(x_e) - \overline{H(x)}]^2 \right\rangle}, $$
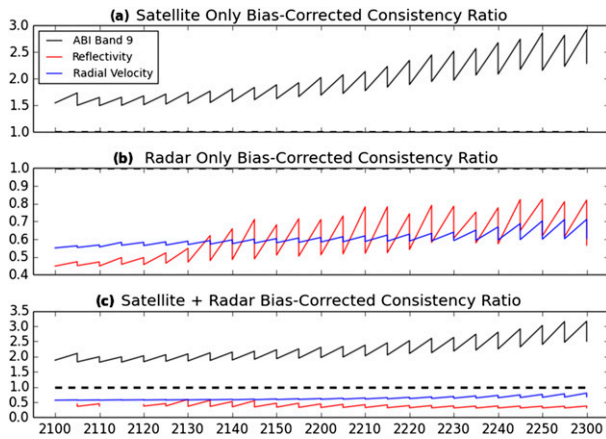$$ (2) $$

FIG. 4. Consistency ratio during the 2-h assimilation period for the (a) SAT, (b) RAD, and (c) SATRAD experiments for the ABI 6.95-μm brightness temperatures (black lines), radar reflectivity (red lines), and radial velocity (blue lines) observations.

where σ_{obs} is the observation error standard deviation and E is the number of ensemble members. They are used to compute the consistency ratio (CR) as an assessment of the assimilation system that compares the actual ensemble spread to the optimal ensemble spread (e.g., Dowell et al. 2004; Aksoy et al. 2009; Dowell and Wicker 2009; Jones et al. 2015):

$$\text{CR} = (\text{Total Spread})^2/(\text{RMSI})^2. \qquad (3)$$

A CR of 1.0 is desired because the total spread should equal the RMSI in an ideal situation for a given observation type. Values less (greater) than 1.0 indicate too little (too much) ensemble spread and/or too small (large) of observation error variance. Figure 4 shows the CR time series computed during the assimilation period for the SAT, RAD, and SATRAD experiments. The satellite observations consistently have a CR > 1, indicating that larger-than-optimal observation errors were used or that there is too much spread in the model variables that the infrared brightness temperatures are most sensitive to (primarily water vapor and clouds). The radar reflectivity and radial velocity observations, however, have a CR < 1, which suggests they could benefit from increased ensemble spread or a larger observation error.

b. Brightness temperature assimilation statistics and final analysis

To assess the impact of the satellite and radar observations on the cloud and water vapor fields in the middle and upper troposphere, the bias and RMSE for the ABI 6.95-μm brightness temperatures for each assimilation cycle are shown in Fig. 5. The 500-hPa water vapor and
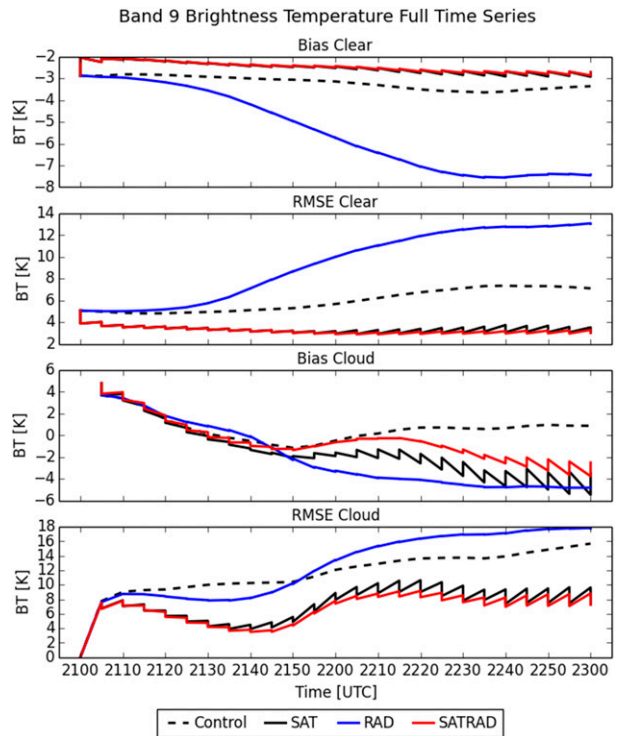

FIG. 5. ABI band 9 (6.95 μm) brightness temperature (K) bias and RMSE time series during the assimilation period for the CTRL (dashed line), SAT (black line), RAD (blue line), and SATRAD (red line) experiments. The top two panels show the statistics where the TRUTH simulation is cloud-free, whereas the bottom two panels show the statistics where the TRUTH simulation has clouds.

total cloud mixing ratio (sum of the cloud water, rainwater, cloud ice, snow, and graupel mixing ratios) from the TRUTH simulation at the end of the assimilation period is shown in Figs. 6 and 7 along with the differences between TRUTH and the ensemble mean for each assimilation experiment. For reference, the final 6.95-μm brightness temperature analyses are shown in the first column of Fig. 8.

For the clear-sky grid points, the bias and RMSE are smallest during the SAT and SATRAD cases and largest during the RAD case (Fig. 5). The RMSE was also smallest for the cloudy grid points when the satellite brightness temperatures were assimilated; however, the bias was slightly larger than the CTRL case and with the opposite sign. The reversal in bias is primarily due to the lack of clouds in the CTRL case over southeastern Kansas and northeastern Missouri (Fig. 8b). The smaller RMSE during the SAT and SATRAD cases was primarily due to a more accurate depiction of the structure and location of the cloud field (Figs. 7, 8), with some improvements also evident in the water vapor field in clear-sky areas (Figs. 6, 8c). For the RAD case, large
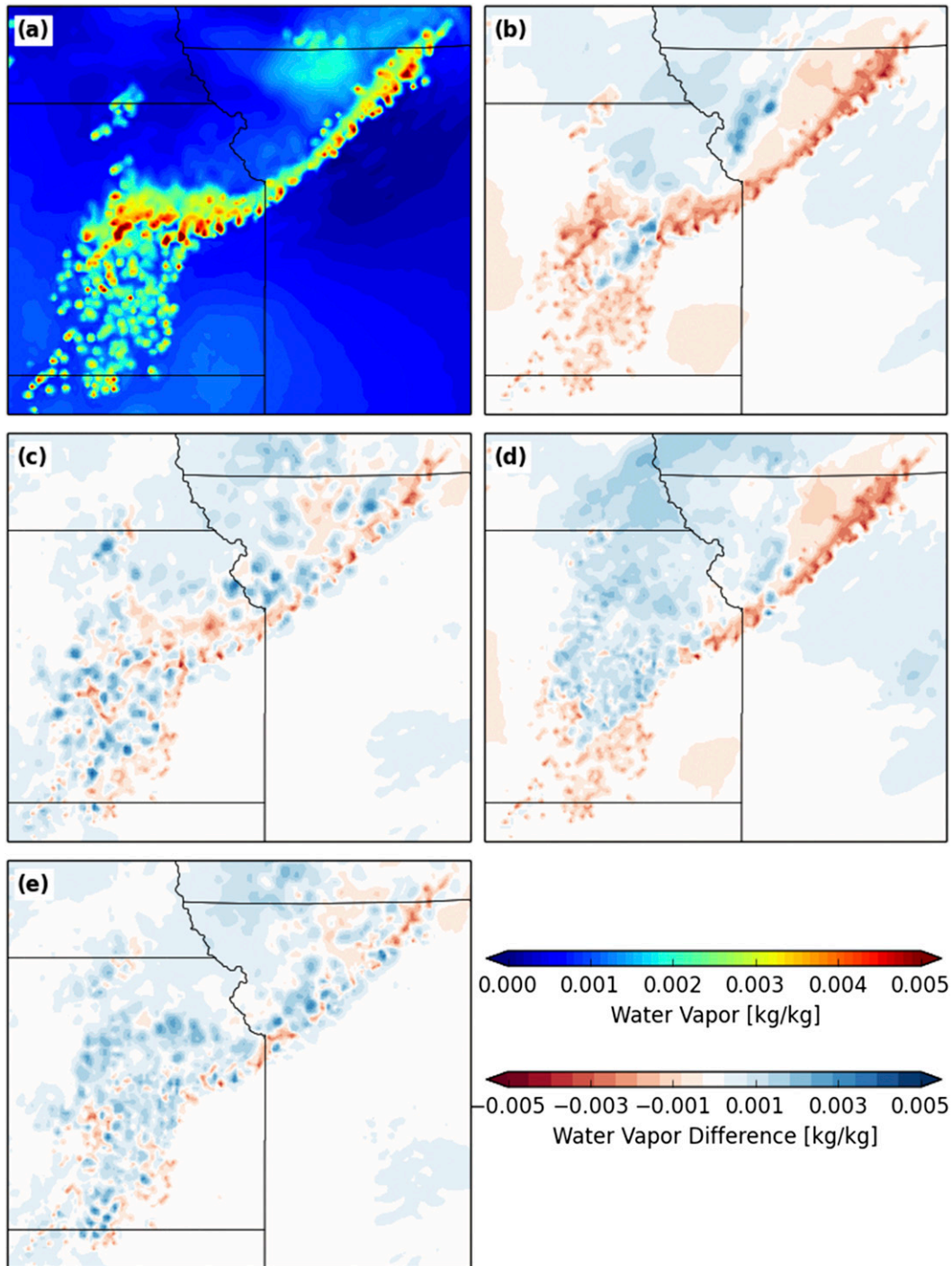
FIG. 6. (a) The 500-hPa water vapor mixing ratio ($kg\,kg^{-1}$) from the TRUTH simulation. (b)–(e) The 500-hPa water vapor mixing ratio difference ($kg\,kg^{-1}$) between the TRUTH simulation and the CTRL, SAT, RAD, and SATRAD assimilation cases, respectively. All images are valid at 2300 UTC.

errors developed by the end of the assimilation period because of the expansion of upper-level clouds to the north of the thunderstorms that were not present in the TRUTH simulation (Figs. 8a,e). These extensive

upper-level clouds had developed because the radar assimilation led to excessive water vapor (Fig. 6d) and cloud mass (Fig. 7d) within the thunderstorms over eastern Kansas that was then transported to the north
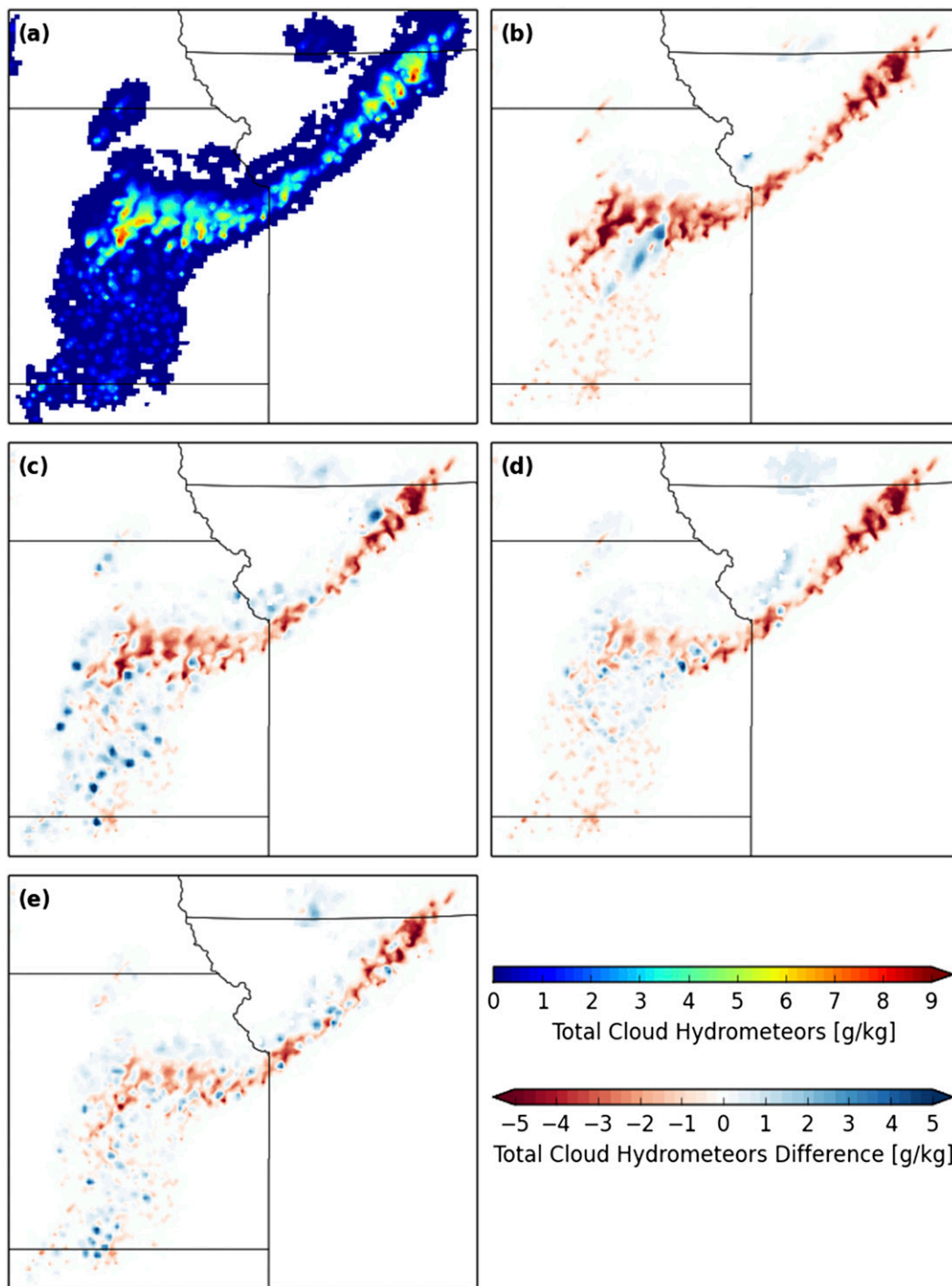
FIG. 7. (a) The 500-hPa total cloud hydrometeor mixing ratio $(g\,kg^{-1})$ from the TRUTH simulation. This is the sum of the cloud water, rainwater, cloud ice, snow, and graupel mixing ratios. (b)–(e) The 500-hPa total cloud hydrometeor mixing ratio difference $(g\,kg^{-1})$ between the TRUTH simulation and the CTRL, SAT, RAD, and SATRAD assimilation cases, respectively. All images are valid at 2300 UTC.
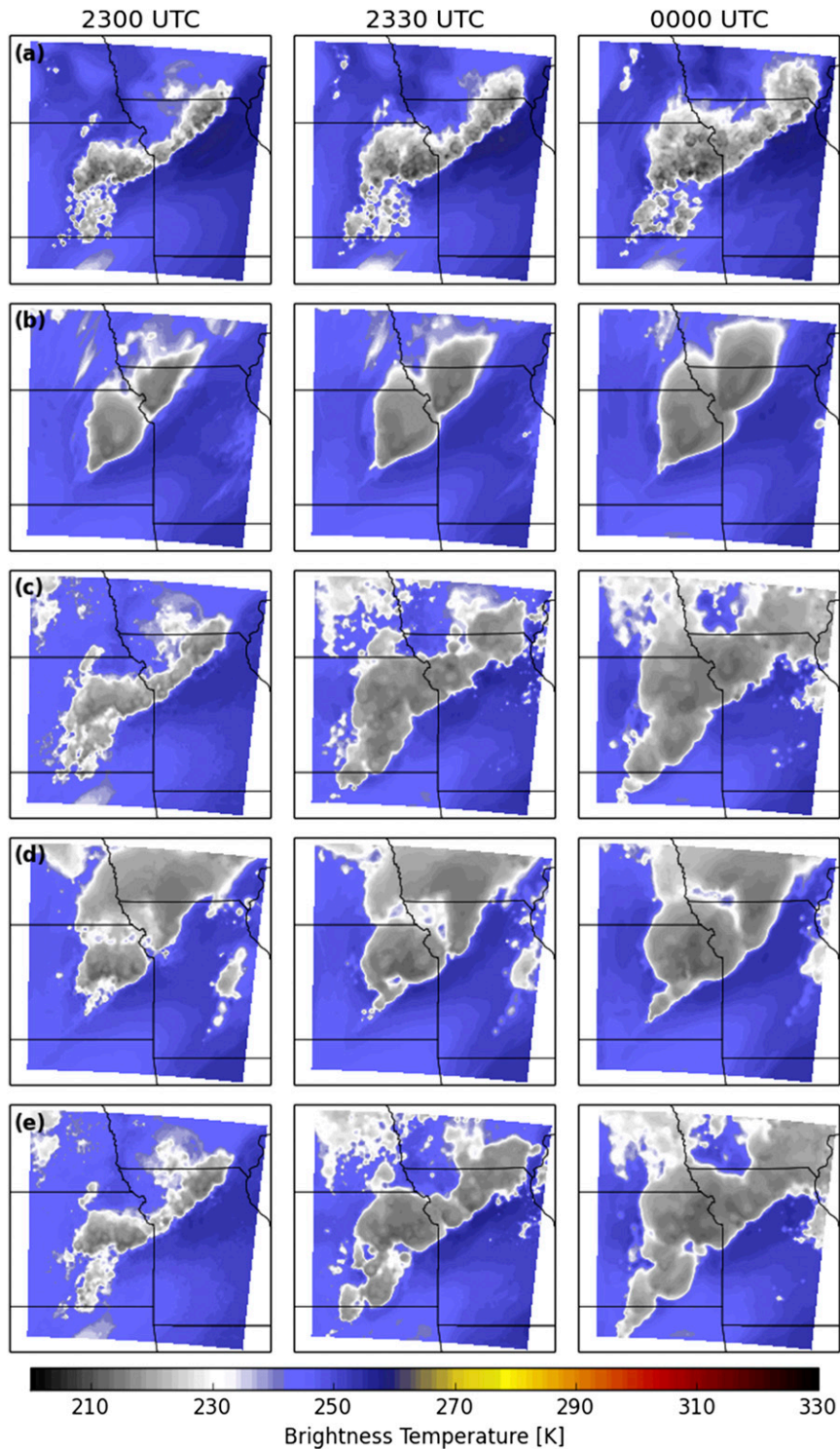
FIG. 8. GOES-R ABI band 9 (6.95 μm) brightness temperatures during the final 1-h forecast at 2300, 2330, and 0000 UTC from the (a) TRUTH simulation, and from the ensemble mean for the (b) CTRL, (c) SAT, (d) RAD, and (e) SATRAD experiments, respectively.

and east by the southwesterly upper level winds present across the region. The large wet bias in the RAD case (Fig. 6d) indicates that some of the cloud information was being incorrectly projected onto the water vapor field. It is possible, though, that these errors could have been constrained if more radar observations were assimilated in the surrounding clear-sky regions. Assimilation of the satellite observations did not lead to excessive midlevel moistening along the western half of the convective line, though the analysis was slightly drier than the TRUTH simulation. Substantial moistening occurred farther to the east across northern Missouri (Fig. 6c), however, which helped promote the more extensive development of thunderstorms across this region in the SAT and SATRAD cases.

c. Ensemble mean 1-h brightness temperature and composite reflectivity forecasts

After completing the 2-h assimilation period, a 1-h ensemble forecast was run for each assimilation experiment using the final ensemble analyses obtained at the end of the assimilation period. Figure 8 shows the ensemble mean 6.95-μm brightness temperatures for each experiment at 30-min intervals during the forecast period with the corresponding ensemble mean WSR-88D composite reflectivity over the same time period shown in Fig. 9. The top row in each figure shows the evolution of TRUTH from 2300 to 0000 UTC, over which time the upper-level clouds expanded in TRUTH (Fig. 8a) as the thunderstorms intensified (Fig. 9a).

The CTRL experiment (Fig. 9b) contains a broken line of thunderstorms across eastern Kansas and northwestern Missouri near a surface moisture boundary; however, they do not have the same structure, extent, or placement as the storms in the TRUTH simulation. The storms over northwestern Missouri are located too far to the west of the actual line of storms and maintain the westward displacement during the 1-h forecast. The CTRL case shows two distinct regions of cloud associated with the two storm clusters seen in the radar reflectivity, but the brightness temperatures do not change much during the forecast except to show a spreading of the cloud anvils. The coldest cloud tops are not as cold or as well defined as those seen in the TRUTH (Fig. 8a) simulation.

The line of storms that extends from Kansas City northeastward into southern Iowa has much better placement, extent, and structure for both the brightness temperatures (Fig. 8c) and the reflectivity (Fig. 9c) in the SAT experiment. The cloud shape is very similar to TRUTH at 2300 UTC, and the reflectivity structure of the storms in eastern Kansas is relatively well reproduced; however, the lighter showers across southern

Kansas and northern Oklahoma are too strong compared with TRUTH. Most of the storms do not maintain their strength during the 1-h forecast and do not increase in extent as found in TRUTH. There are still storms in eastern Kansas and a hint of the line that extends through northern Missouri, though quite weakened, at the end of the forecast. The SAT experiment captures the precipitation in eastern Nebraska, but with too broad of an extent of 5–30 dBZ reflectivity, and these showers dissipate prior to the end of the forecast period.

The cloud tops in eastern Kansas also have the same general shape in the RAD experiment (Fig. 8d) as in the TRUTH, but differences are large elsewhere in the domain. The horizontal structure of the composite reflectivity in eastern Kansas is better captured by the RAD experiment (Fig. 9d) than the SAT, though with higher maximum reflectivity than the storms in TRUTH. Even though the radar observations improve the radar analysis in eastern Kansas, they do not improve the corresponding satellite analysis over the SAT experiment because they do not capture as much of the cloud-top detail. The line of storms is not reproduced in Missouri, however, which is likely because of the sparseness of WSR-88D radar data available in that region, especially in the lower levels (Fig. 1). The northeastern portion of Missouri does not have WSR-88D radar coverage below 10 000 ft (3048 m) above ground level, so no radars are able to give sufficient coverage in the low levels for that region. The weaker storms across southern Kansas are also not reproduced, even though observations from the Wichita radar were assimilated. The satellite observations, however, were able to detect these cloud features given their greater sensitivity to small cloud particles and were thus able to recreate them during the assimilation period. Similar to the SAT experiment, the strength of the storms produced in the RAD analysis is not maintained during the 1-h forecast period and the reflectivity does not increase in coverage as in TRUTH, even though the upper-level anvil clouds continue to spread unhindered.

The SATRAD experiment starts with and maintains the best cloud structure and spatial extent throughout the forecast period (Fig. 8e). It also produces the most accurate depiction of the TRUTH reflectivity forecast (Fig. 9e) as it best captures the structure of the storms in eastern Kansas and the line of storms extending through northern Missouri. The strength of the precipitation in southern Kansas that is overdone by the SAT experiment and too weak in the RAD case is much closer to that shown in TRUTH. In addition, all of these features are better maintained during the 1-h forecast. Therefore, these results indicate that both observation types provide useful information and produce the most accurate results when assimilated together.
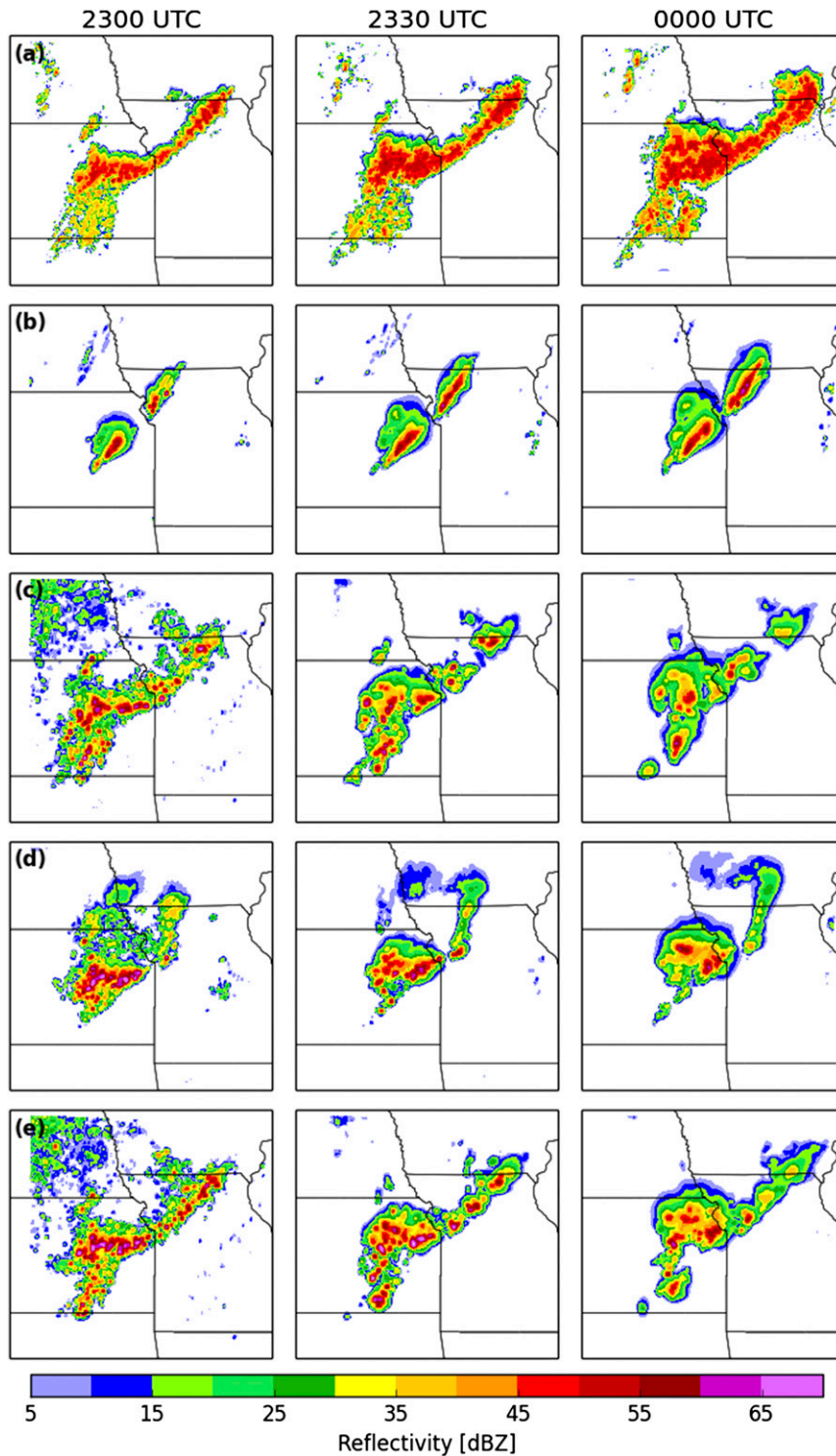
FIG. 9. Composite radar reflectivity (dBZ) during the final 1-h forecast at 2300, 2330, and 0000 UTC from the (a) TRUTH simulation, and from the ensemble mean for the (b) CTRL, (c) SAT, (d) RAD, and (e) SATRAD experiments, respectively.
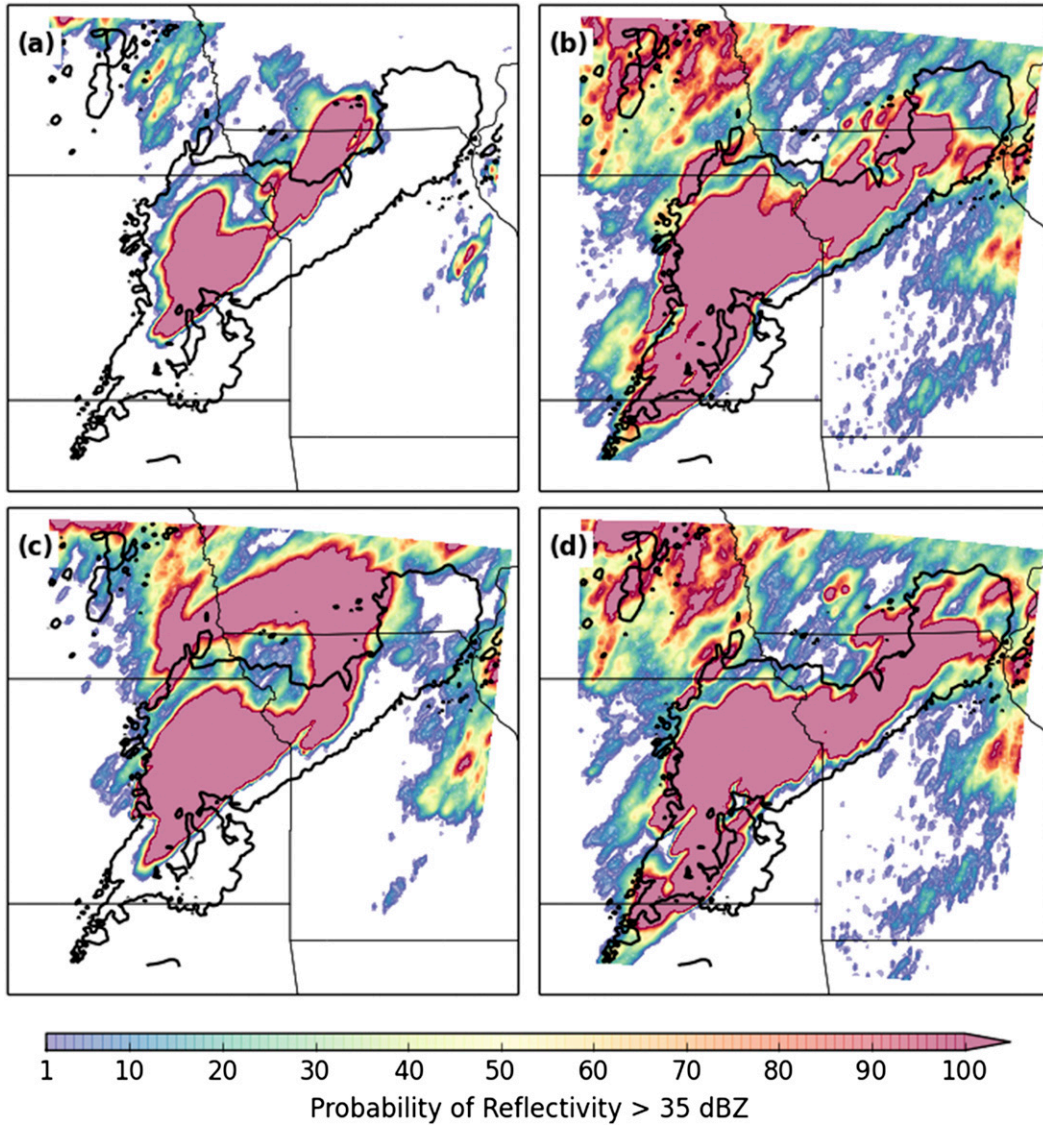
FIG. 10. Probability of composite radar reflectivity >35 dBZ during the 1-h forecast period for the (a) CTRL, (b) SAT, (c) RAD, and (d) SATRAD experiments. The composite reflectivity >35 dBZ swath from the TRUTH simulation is indicated by the thick black contour overlaid on each panel.

d. Probabilistic 1-h composite reflectivity forecasts

Figure 10 shows the probability of an ensemble member having a composite radar reflectivity >35-dBZ during the 1-h forecast for each experiment, with the >35-dBZ reflectivity swath for TRUTH indicated by the black contour. The assimilation of satellite or radar observations separately produced high probabilities that were more consistent with the spatial extent of the TRUTH than when no data were assimilated during the CTRL case. The satellite brightness temperature assimilation better captured the high reflectivity values across Missouri and southern Kansas. The strengths of each observation type work together in the SATRAD

experiment to render the most accurate forecast probabilities of the four experiments. Thus, it has both the best reflectivity forecast from the ensemble mean and the best probabilistic reflectivity forecast based on the 50-member ensemble.

e. Environmental impacts

The maintenance of the storms during the final 1-h forecast is dependent on the model environment. The difference between the experiment and TRUTH total column water vapor is shown in Fig. 11 for the CTRL, SAT, RAD, and SATRAD experiments. All of the cases are too dry in the low-level inflow region to the south of
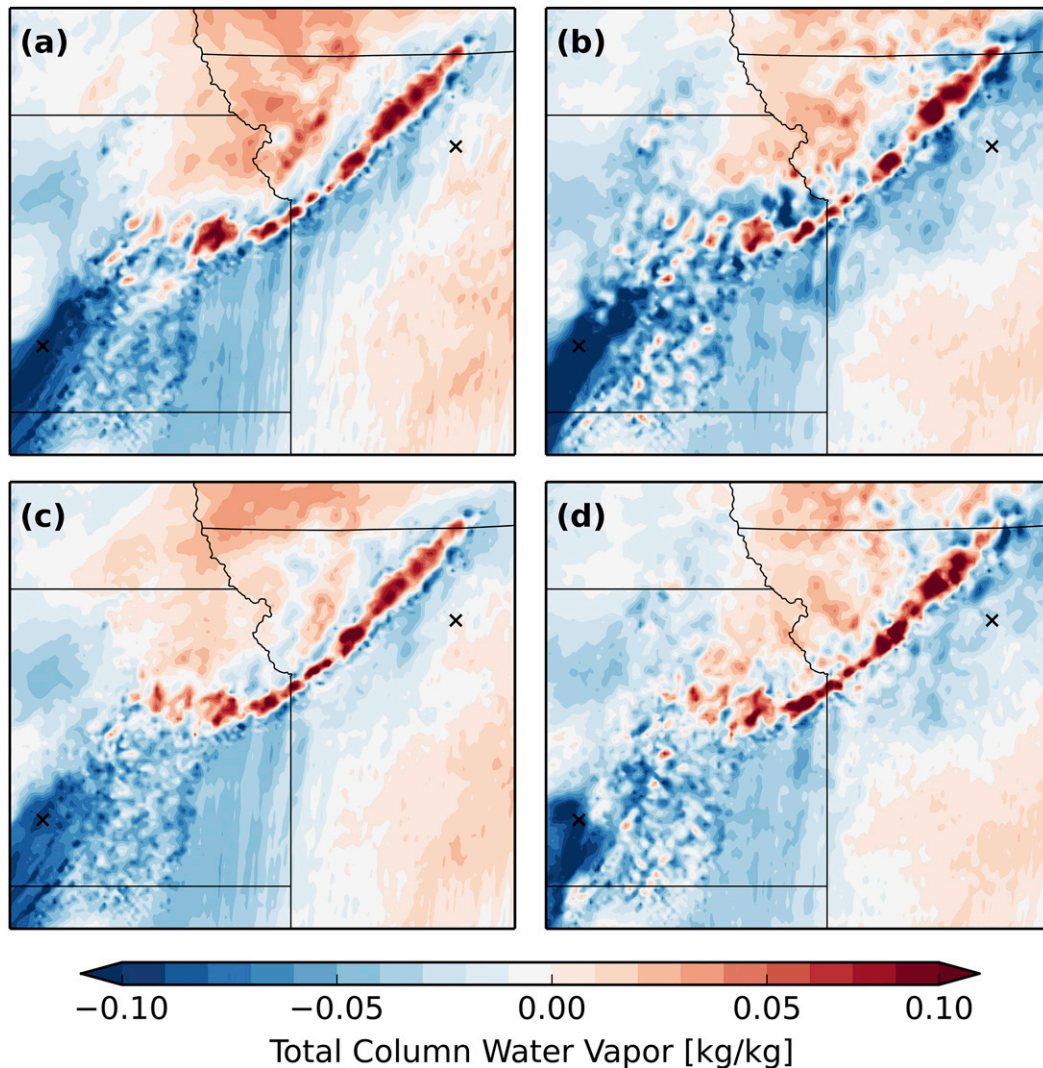
FIG. 11. Ensemble-mean total column water vapor difference (experiment minus TRUTH) at 2300 UTC for the (a) CTRL, (b) SAT, (c) RAD, and (d) SATRAD experiments. The black "×" indicates the location of the skew *T*–log*p* diagrams shown in Fig. 12.

the storms. The satellite assimilation helps reduce the dry bias in southeastern Kansas while increasing it in north-central Missouri. The use of the GFS for the initial and lateral boundary conditions instead of the NAM results in a warm, moist boundary region in the experiment background that extends farther north than in TRUTH, which shows in the overabundance of total column water vapor north of the storms in all of the experiments. At the same time, the dryline from southern Kansas into Oklahoma is more defined and located farther east in the experiments than the TRUTH. The RAD case reduces the dry bias in the southwestern corner of the domain more effectively than SAT, primarily below 650 hPa (not shown).

The black crisscross (×) in Fig. 11 indicates the location of the environmental sounding shown in Fig. 12. Figure 12a shows the drying that the assimilation of the ABI 6.95-μm brightness temperatures in the SAT and SATRAD experiments produced throughout much of the troposphere below 450 hPa at that location, particularly between 300 and 600 hPa. This is the region where the 6.95-μm clear-sky weighting function peaks and so is most sensitive to atmospheric water vapor and is where the largest impact would be expected. Though the drying brings the SAT moisture sounding closer to TRUTH above 500 hPa, it results in a small dry bias below that level. The CTRL profile is moister than TRUTH through most of the column, and the RAD experiment does not change the sounding because the radar
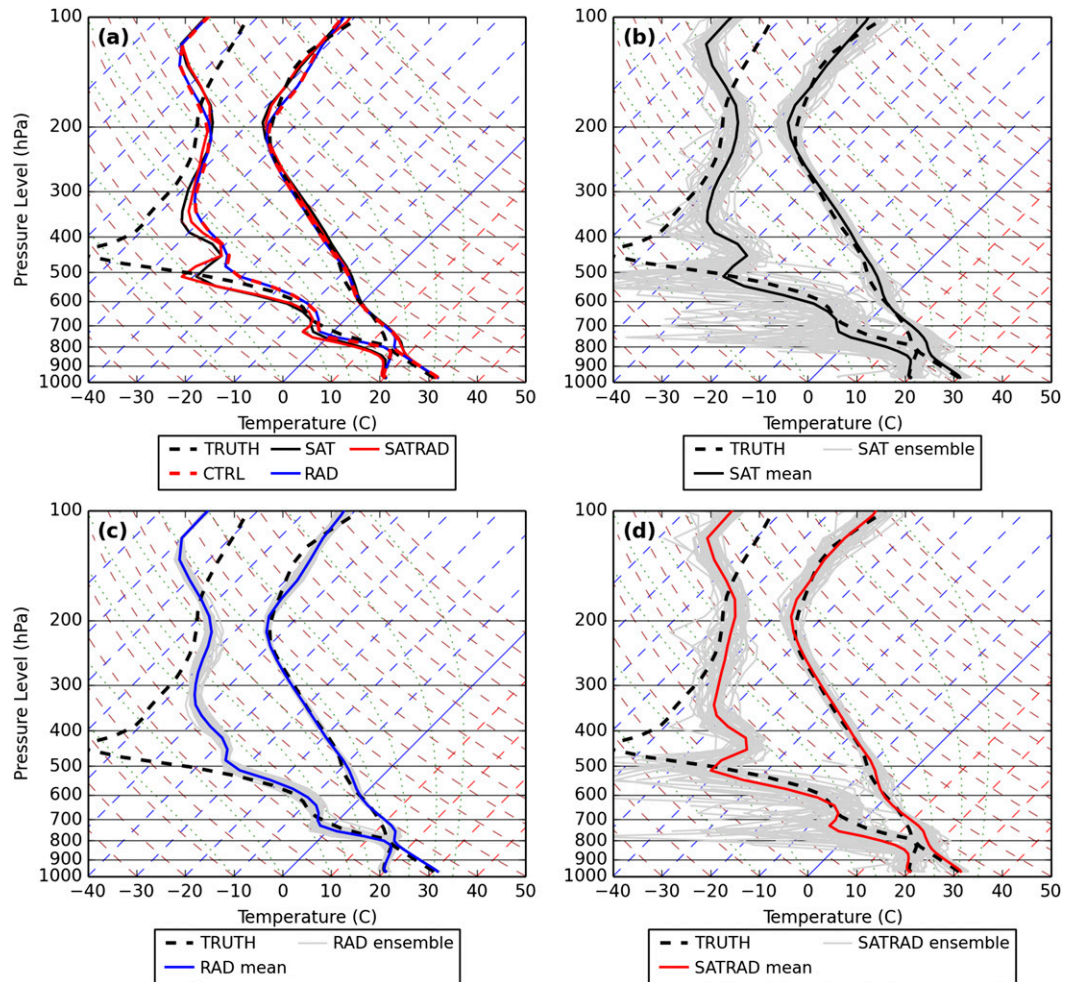
FIG. 12. Skew *T*–log*p* diagrams for a location in northeast Missouri just southeast of the storms at 2300 UTC showing (a) the TRUTH and ensemble means for each experiment; (b) the ensemble mean and individual ensemble members (gray) from the SAT experiment; (c) as in (b), but for the RAD experiment; and (d) as in (b), but for the SATRAD experiment.

observations are sparse surrounding this location. There is also more spread within the ensemble soundings when the brightness temperatures are assimilated than when radar observations are assimilated, so the assimilated radar observations have less of an impact with more weight given to the prior model state.

Low-level moisture provides fuel for storms and surface moisture convergence, and boundaries are often favored locations for storm initiation. Figure 13a shows the 2-m dewpoint temperature and 10-m winds for the TRUTH at 2300 UTC. The remaining panels (Figs. 13b–e) show the 2-m dewpoint temperature difference between each experiment and the TRUTH simulation at that time, with the 10-m winds overlaid on each panel. The assimilation of satellite observations reduces the dry bias at the surface in the storm inflow region in southern Kansas and western Missouri as well as the

moist bias in eastern Missouri. The 6.95-μm channel peaks in the midtroposphere, but the observations still impact the surface fields because no vertical covariance localization is used during their assimilation. The air behind the dryline in southern Kansas is too dry, and the dryline is located too far east in the CTRL experiment. Radar assimilation improves it somewhat because the assimilation of radial velocity impacts the low-level moisture advection. However, the improvements are not as large as when the brightness temperatures are assimilated. The most accurate surface dewpoint temperatures are obtained when both observation types are assimilated.

Figure 14a shows the 2-m temperature and 10-m wind for the TRUTH at 2300 UTC. The cold pool generated by the storms can be seen in the 300 K and colder region across eastern Kansas and northwestern Missouri, with
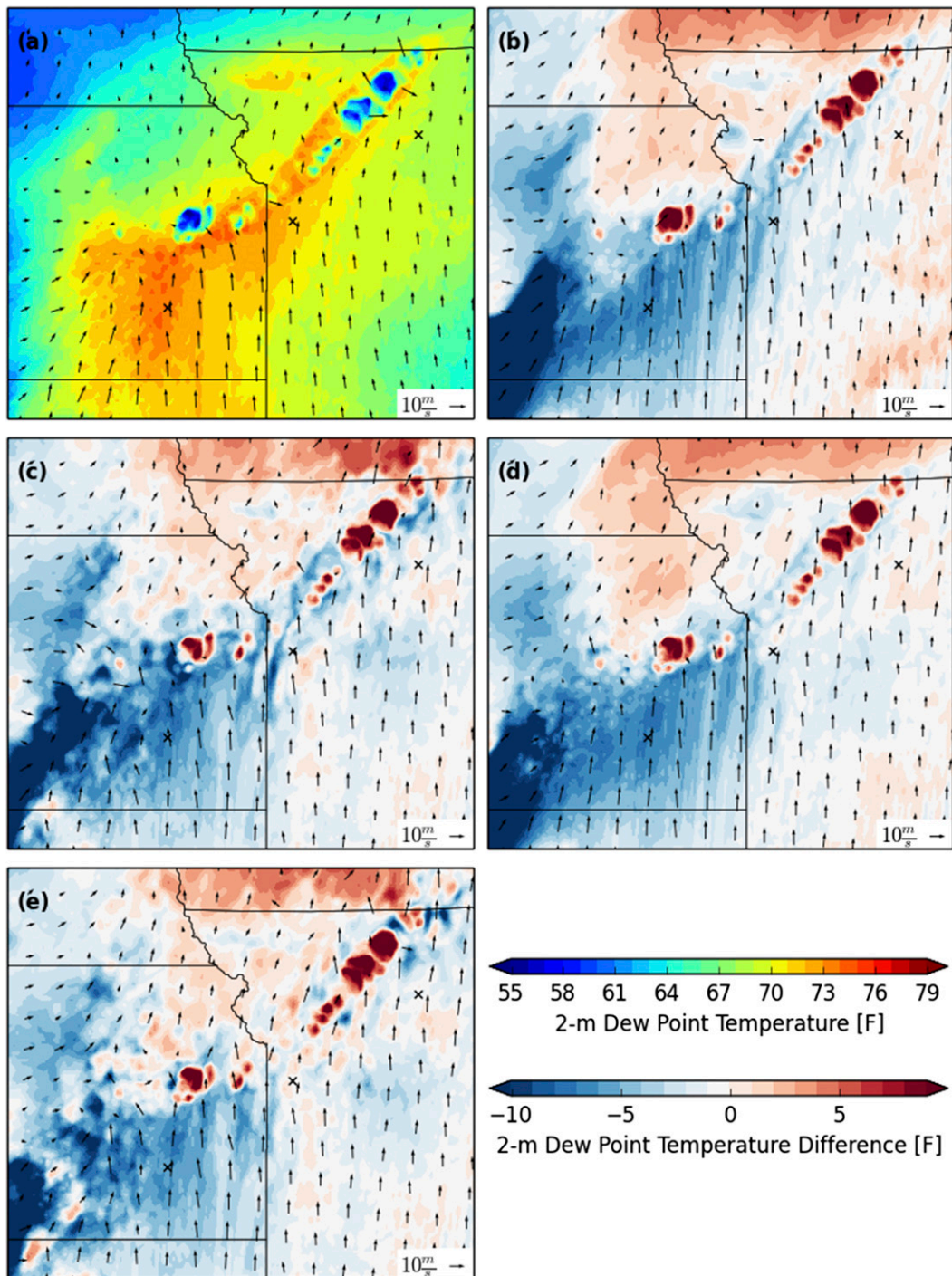
FIG. 13. (a) The 2-m dewpoint temperature (K) and 10-m winds (m s^{-1}; arrows) from the TRUTH simulation. (b)–(e) The 10-m winds (m s^{-1}) and 2-m dewpoint temperature difference (K) between the TRUTH simulation and the CTRL, SAT, RAD, and SATRAD assimilation cases, respectively. All images are valid at 2300 UTC.

the surface winds diverging from the cold pool as the colder, denser air flows outward from the strongest storms. The rest of the panels (Figs. 14b–e) show the difference between the 2-m temperatures of the experiment and

the TRUTH at 2300 UTC, with blue showing where the TRUTH is colder and red where the experiment is colder. The 10-m winds from each experiment are overlaid. The cold pools from TRUTH stand out in the
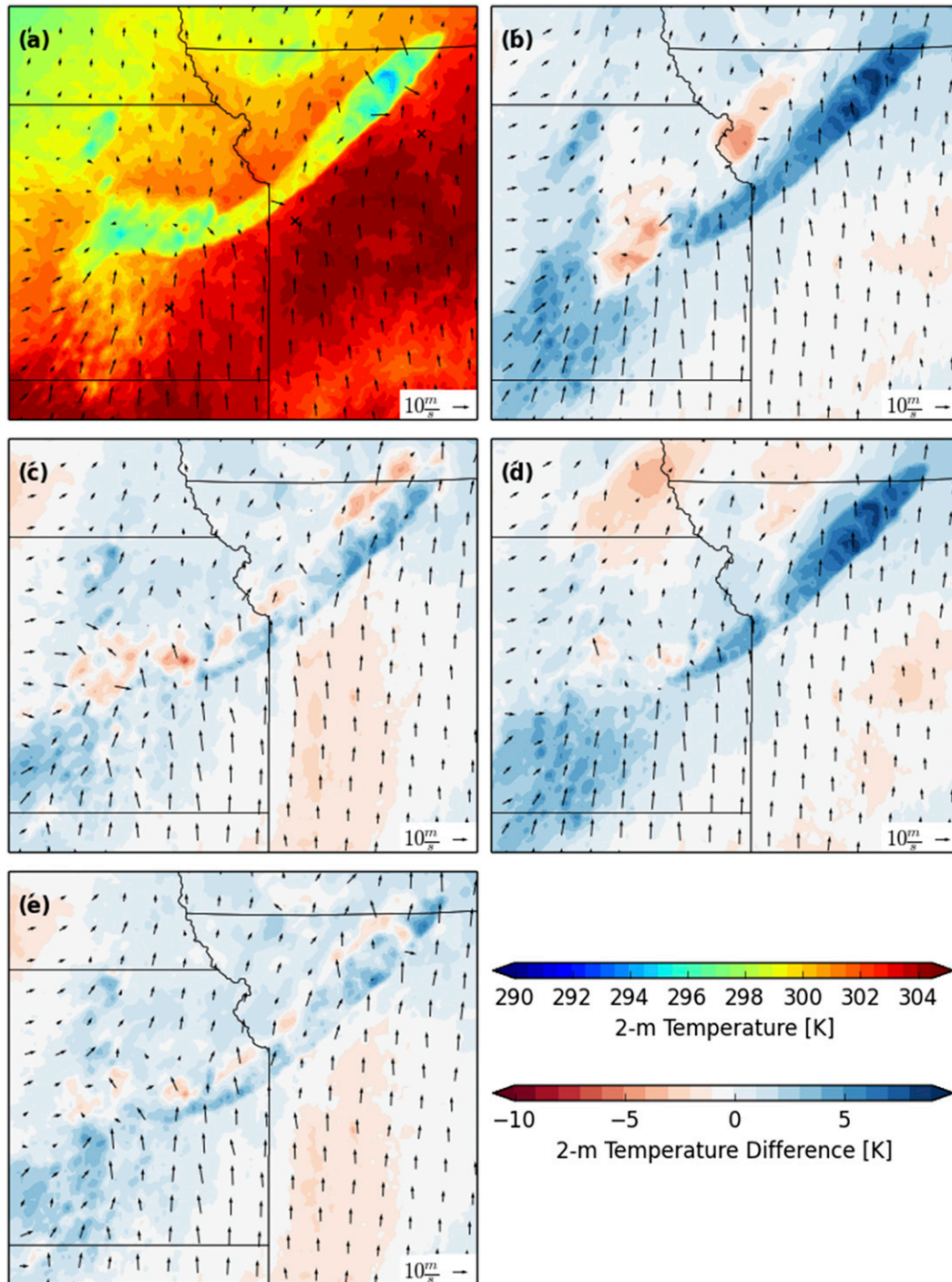
FIG. 14. (a) The 2-m temperature (K) and 10-m winds (m s^{-1}; arrows) from the TRUTH simulation. (b)–(e) The 10-m winds (m s^{-1}) and 2-m temperature difference (K) between the TRUTH simulation and the CTRL, SAT, RAD, and SATRAD cases, respectively. All images are valid at 2300 UTC.

CTRL and RAD experiments in dark blue in Missouri where no cold pools were analyzed. The SAT experiment reduces the surface temperature difference in the cold pool, but it is still too warm in locations where the storms are not as strong and too cold on the north side of the cold pool where the clouds are thicker than in the TRUTH. The SATRAD experiment brings the surface temperatures closest to TRUTH, though they are still

too warm for much of the cold pool. This suggests that either none of the experiment analyses have strong enough storms or the difference in the microphysics used in the TRUTH and experiments could be influencing the strength of the cold pools and the formation of new updrafts along the cold pool leading edge. Some studies have shown that single-moment microphysics, such as the WSM6 used in the TRUTH simulation, may produce colder cold pools than multimoment schemes since they produce more small drops in the lower levels that evaporate more readily (e.g., Dawson et al. 2010, 2015). However, those results are not conclusive, as shown by Wheatley et al. (2014), and so may not explain the differences in cold pool strength here.

The combination of higher 2-m temperature and moisture leads to larger values of surface-based convective available potential energy (CAPE) in TRUTH. There is a large disparity in the magnitude and distribution of CAPE between TRUTH and the experiments (Fig. 15). TRUTH has the highest values of CAPE where the southerly low-level winds are advecting very moist, warm air into southeastern Kansas and western Missouri. The storms, whose cooling effect is evident in the CAPE minimum, form along the pooling of the higher CAPE values during the assimilation period. Unlike the TRUTH simulation, the experiments have relatively low CAPE across Kansas and extend the region of CAPE $> 3000 \, \mathrm{J \, kg^{-1}}$ too far north into Iowa. The assimilation of brightness temperatures increases the CAPE in the storm inflow region, providing more fuel for the storms. The SATRAD experiment increases the CAPE the most and brings the structure of the CAPE closer to TRUTH, at least in the immediate inflow region of the storms in northwestern Missouri. The GFS analysis used to initialize the experiments has the warm, moist air extending farther north into Iowa than the NAM analysis used to initialize the TRUTH simulation (not shown), which influences the spatial extent and location of the higher CAPE values.

8. Conclusions and discussion

An OSSE was performed that assimilated synthetic GOES-R ABI 6.95-μm brightness temperatures and Doppler radar reflectivity and radial velocity observations on a 4-km-resolution ARW model domain using the DART ensemble data assimilation system. The observations were assimilated every 5 min during a 2-h period before a 1-h ensemble forecast was generated from the final ensemble analyses. A simple bias correction was used for the clear-sky brightness temperatures in order to reduce a cold bias present at the beginning of the assimilation experiments. A horizontal localization

radius half-width of 28 km was found to work well when assimilating the brightness temperatures. The assimilation of the radar observations provided the best storm structure across eastern Kansas, but they were not available throughout the model domain and so were not able to reproduce the entire storm system. However, the satellite brightness temperatures covered the entire domain and were able to reproduce the general structure of the storms, including those not produced by the radar assimilation. The assimilation of the satellite brightness temperatures improved the structure of the water vapor field in the clear-sky regions and resulted in cloud tops and structure in the analysis in relatively good agreement with TRUTH. The most accurate analysis and forecast resulted from analyses produced when both GOES-R ABI brightness temperatures and Doppler radar observations were assimilated. Where no or sparse radar observations were available, the satellite observations were able to reproduce the storms and improve the storm environment. At the same time, the radar observations were able to refine the thunderstorm structure where they were available. Thus, these results provide evidence that satellite and radar observations provide complementary information.

There were several differences between the setup of the TRUTH simulation and the model experiments that kept the OSSE from being an identical twin experiment. Different datasets were used to initialize the TRUTH simulation and the assimilation experiments, the NAM for the former and the GFS for the latter. This resulted in differences in the atmospheric environment that were not completely overcome through the assimilation of the satellite and radar observations. Different cloud microphysics and radiation schemes were also used, in addition to different forward radiative transfer models for creating and assimilating the synthetic brightness temperatures. Though eliminating the possibility of performing an "identical twin" experiment, all of these differences made it more difficult to determine the exact impacts of the assimilation experiments. However, they may also help create an environment that is more analogous to an actual operational setting. The assimilation of surface observations during the 2-h assimilation period would likely have helped improve the surface environment, which in turn may have improved the analyses and forecasts.

Overall, this study demonstrates the advantages of assimilating GOES-R ABI 6.95-μm brightness temperatures in a high-resolution model, both alone and in combination with Doppler radar reflectivity and radial velocity observations. The major features of a complex of severe storms were reproduced in the analysis, and the forecast accuracy was improved when the brightness temperatures were assimilated. A more sophisticated
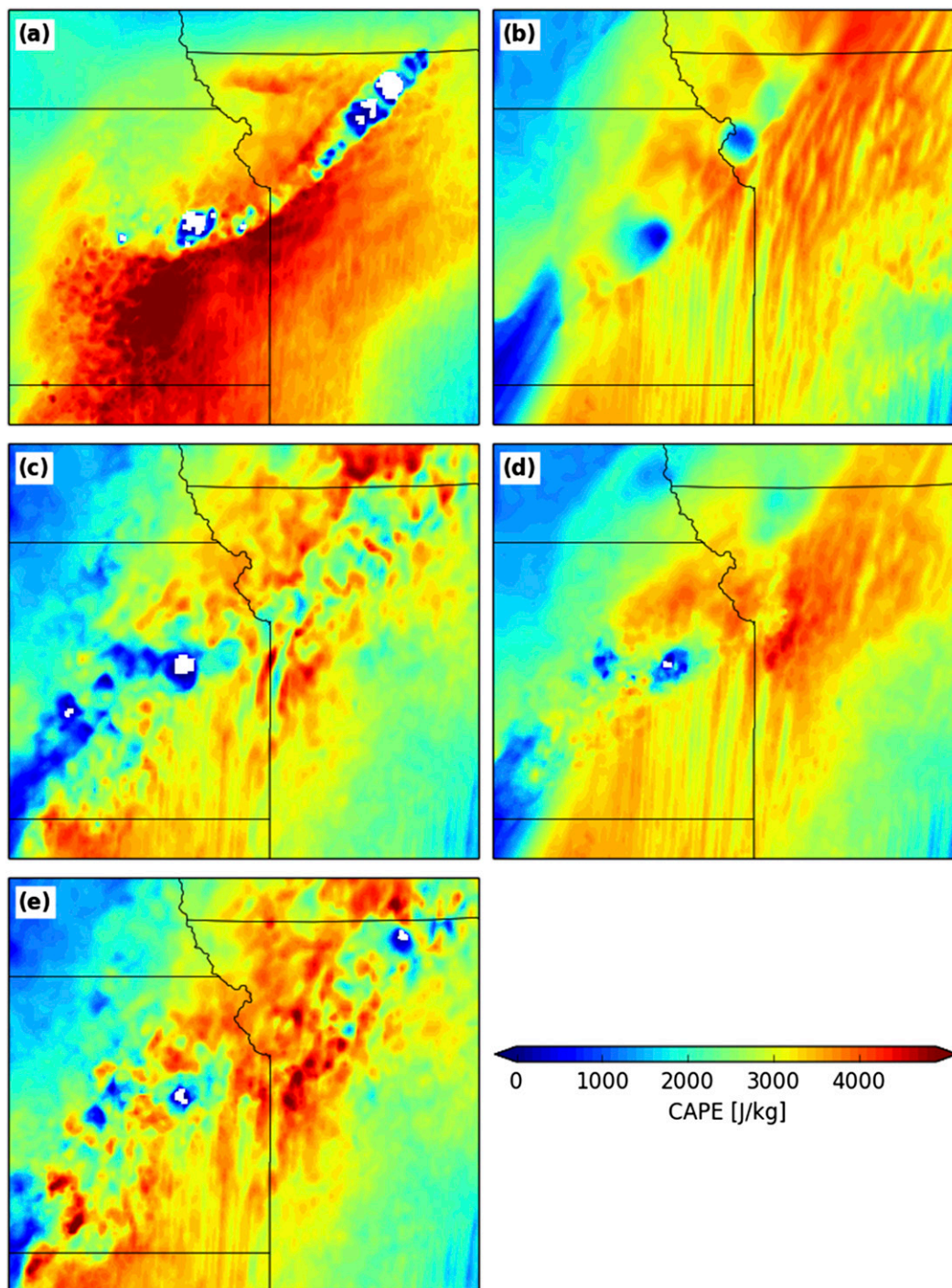
FIG. 15. (a) Surface-based CAPE from the TRUTH simulation. Differences in surface-based CAPE between TRUTH and the (b) CTRL, (c) SAT, (d) RAD, and (e) SATRAD experiments. All images are valid at 2300 UTC.

bias correction method and the assimilation of additional ABI bands may further improve these results. Though computationally expensive, these experiments demonstrate the feasibility of assimilating high-resolution satellite and radar observations and are relevant to other experimental convection-resolving data assimilation systems under development (e.g., Wheatley et al. 2015; Jones et al. 2016).

REFERENCES

Aksoy, A., D. C. Dowell, and C. Snyder, 2009: A multicase comparative assessment of the ensemble Kalman filter for assimilation of radar observations. Part I: Storm-scale analysis. *Mon. Wea. Rev.*, **137**, 1805–1824, doi:10.1175/2008MWR2691.1.

Anderson, J. L., 2001: An ensemble adjustment Kalman filter for data assimilation. *Mon. Wea. Rev.*, **129**, 2884–2903, doi:10.1175/1520-0493(2001)129<2884:AEAKFF>2.0.CO;2.

——, 2007: An adaptive covariance inflation error correction algorithm for ensemble filters. *Tellus*, **59A**, 210–224, doi:10.1111/j.1600-0870.2006.00216.x.

——, 2009: Spatially and temporally varying adaptive covariance inflation for ensemble filters. *Tellus*, **61A**, 72–83, doi:10.1111/j.1600-0870.2008.00361.x.

Andersson, E., and Coauthors, 2005: Assimilation and modeling of the atmospheric hydrological cycle in the ECMWF forecasting system. *Bull. Amer. Meteor. Soc.*, **86**, 387–402, doi:10.1175/BAMS-86-3-387.

Atlas, R., E. Kalnay, and M. Halem, 1985: Impact of satellite temperature sounding and wind data on numerical weather prediction. *Opt. Eng.*, **24**, 242341, doi:10.1117/12.7973481.

Bauer, P., G. Ohring, C. Kummerow, and T. Auligne, 2011: Assimilating satellite observations of clouds and precipitation into NWP models. *Bull. Amer. Meteor. Soc.*, **92**, ES25–ES28, doi:10.1175/2011BAMS3182.1.

Chen, F., and J. Dudhia, 2001: Coupling an advanced land surface-hydrology model with the Penn State–NCAR MM5 modeling system. Part I: Model implementation and sensitivity. *Mon. Wea. Rev.*, **129**, 569–585, doi:10.1175/1520-0493(2001)129<0569:CAALSH>2.0.CO;2.

Dawson, D. T., M. Xue, J. A. Milbrandt, and M. K. Yau, 2010: Comparison of evaporation and cold pool development between single-moment and multimoment bulk microphysics schemes in idealized simulations of tornadic thunderstorms. *Mon. Wea. Rev.*, **138**, 1152–1171, doi:10.1175/2009MWR2956.1.

——, L. J. Wicker, E. R. Mansell, and R. L. Tanamachi, 2012: Impact of the environmental low-level wind profile on ensemble forecasts of the 4 May 2007 Greensburg, Kansas, tornadic storm and associated mesocyclones. *Mon. Wea. Rev.*, **140**, 696–716, doi:10.1175/MWR-D-11-00008.1.

——, M. Xue, J. A. Milbrandt, and A. Shapiro, 2015: Sensitivity of real-data simulations of the 3 May 1999 Oklahoma City tornadic supercell and associated tornadoes to multimoment microphysics. Part I: Storm- and tornado-scale numerical forecasts. *Mon. Wea. Rev.*, **143**, 2241–2265, doi:10.1175/MWR-D-14-00279.1.

Dowell, D. C., and L. J. Wicker, 2009: Additive noise for storm-scale ensemble data assimilation. *J. Atmos. Oceanic Technol.*, **26**, 911–927, doi:10.1175/2008JTECHA1156.1.

——, F. Zhang, L. Wicker, C. Snyder, and N. A. Crook, 2004: Wind and temperature retrievals in the 17 May 1981 Arcadia,

Oklahoma, supercell: Ensemble Kalman filter experiments. *Mon. Wea. Rev.*, **132**, 1982–2005, doi:10.1175/1520-0493(2004)132<1982:WATRIT>2.0.CO;2.

Dudhia, J., 1989: Numerical study of convection observed during the winter monsoon experiment using a mesoscale two-dimensional model. *J. Atmos. Sci.*, **46**, 3077–3107, doi:10.1175/1520-0469(1989)046<3077:NSOCOD>2.0.CO;2.

Errico, R., P. Bauer, and J.-F. Mahfouf, 2007: Issues regarding the assimilation of cloud and precipitation data. *J. Atmos. Sci.*, **64**, 3685–3798, doi:10.1175/2006JAS2044.1.

Fabry, F., and J. Sun, 2010: For how long should what data be assimilated for the mesoscale forecasting of convection and why? Part I: On the propagation of initial condition errors and their implications for data assimilation. *Mon. Wea. Rev.*, **138**, 242–255, doi:10.1175/2009MWR2883.1.

Gao, J., and D. Stensrud, 2012: Assimilation of reflectivity data in a convective-scale, cycled 3DVAR framework with hydrometeor classification. *J. Atmos. Sci.*, **69**, 1054–1065, doi:10.1175/JAS-D-11-0162.1.

Gaspari, G., and S. E. Cohn, 1999: Construction of correlation functions in two and three dimensions. *Quart. J. Roy. Meteor. Soc.*, **125**, 723–757, doi:10.1002/qj.49712555417.

Geer, A. J., and P. Bauer, 2011: Observation errors in all-sky data assimilation. *Quart. J. Roy. Meteor. Soc.*, **137**, 2024–2037, doi:10.1002/qj.830.

Han, Y., P. van Delst, Q. Liu, F. Weng, B. Yan, R. Treadon, and J. Derber, 2006: Community Radiative Transfer Model (CRTM): Version 1. NOAA Tech. Rep. NESDIS 122, 33 pp. [Available online at http://www.star.nesdis.noaa.gov/sod/sst/micros/pdf/CRTM_v1_NOAAtechReport-1.pdf.]

Harnisch, F., M. Weissmann, and Á. Periáñez, 2016: Error model for the assimilation of cloud-affected infrared satellite observations in an ensemble data assimilation system. *Quart. J. Roy. Meteor. Soc.*, **142**, 1797–1808, doi:10.1002/qj.2776.

Harris, B. A., and G. Kelly, 2001: A satellite radiance-bias correction scheme for data assimilation. *Quart. J. Roy. Meteor. Soc.*, **127**, 1453–1468, doi:10.1002/qj.49712757418.

Heidinger, A. K., C. O'Dell, R. Bennartz, and T. Greenwald, 2006: The successive-order-of-interaction radiative transfer model. Part I: Model development. *J. Appl. Meteor. Climatol.*, **45**, 1388–1402, doi:10.1175/JAM2387.1.

Hong, S.-Y., and J.-O. J. Lim, 2006: The WRF single-moment 6-class microphysics scheme (WSM6). *J. Korean Meteor. Soc.*, **42**, 129–151.

——, J. Dudhia, and S.-H. Chen, 2004: A revised approach to ice microphysical processes for the bulk parameterization of clouds and precipitation. *Mon. Wea. Rev.*, **132**, 103–120, doi:10.1175/1520-0493(2004)132<0103:ARATIM>2.0.CO;2.

——, Y. Noh, and J. Dudhia, 2006: A new vertical diffusion package with explicit treatment of entrainment processes. *Mon. Wea. Rev.*, **134**, 2318–2341, doi:10.1175/MWR3199.1.

Houtekamer, P. L., and H. L. Mitchell, 2001: A sequential ensemble Kalman filter for atmospheric data assimilation. *Mon. Wea. Rev.*, **129**, 123–137, doi:10.1175/1520-0493(2001)129<0123:ASEKFF>2.0.CO;2.

Hu, M., M. Xue, and K. Brewster, 2006a: 3DVAR and cloud analysis with WSR-88D level-II data for the prediction of Fort Worth tornadic thunderstorms. Part I: Cloud analysis and its impact. *Mon. Wea. Rev.*, **134**, 675–698, doi:10.1175/MWR3092.1.

——, ——, J. Gao, and K. Brewster, 2006b: 3DVAR and cloud analysis with WSR-88D level-II data for the prediction of Fort Worth tornadic thunderstorms. Part II: Impact of radial

velocity analysis via 3DVAR. *Mon. Wea. Rev.*, **134**, 699–721, doi:10.1175/MWR3093.1.

Iacono, M. J., J. S. Delamere, E. J. Mlawer, M. W. Shephard, S. A. Clough, and W. D. Collins, 2008: Radiative forcing by long-lived greenhouse gases: Calculations with the AER radiative transfer models. *J. Geophys. Res.*, **113**, D13103, doi:10.1029/2008JD009944.

Jones, T. A., and D. J. Stensrud, 2015: Assimilating cloud water path as a function of model cloud microphysics in an idealized simulation. *Mon. Wea. Rev.*, **143**, 2052–2081, doi:10.1175/MWR-D-14-00266.1.

——, ——, P. Minnis, and R. Palikonda, 2013a: Evaluation of a forward operator to assimilate cloud water path into WRF-DART. *Mon. Wea. Rev.*, **141**, 2272–2289, doi:10.1175/MWR-D-12-00238.1.

——, J. A. Otkin, D. J. Stensrud, and K. Knopfmeier, 2013b: Assimilation of satellite infrared radiances and Doppler radar observations during a cool season observing system simulation experiment. *Mon. Wea. Rev.*, **141**, 3273–3299, doi:10.1175/MWR-D-12-00267.1.

——, ——, ——, and ——, 2014: Forecast evaluation of an Observing System Simulation Experiment assimilating both radar and satellite data. *Mon. Wea. Rev.*, **142**, 107–124, doi:10.1175/MWR-D-13-00151.1.

——, D. J. Stensrud, L. Wicker, P. Minnis, and R. Palikonda, 2015: Simultaneous radar and satellite data storm-scale assimilation using an ensemble Kalman filter approach for 24 May 2011. *Mon. Wea. Rev.*, **143**, 165–194, doi:10.1175/MWR-D-14-00180.1.

——, K. Knopfmeier, D. Wheatley, G. Creager, P. Minnis, and R. Palikondo, 2016: The NSSL Multiscale Ensemble. Part II: Combined radar and satellite assimilation. *Wea. Forecasting*, **31**, 297–327, doi:10.1175/WAF-D-15-0107.1.

Jung, Y., M. Xue, and M. Tong, 2012: Ensemble Kalman filter analyses of the 29–30 May 2004 Oklahoma tornadic thunderstorm using one- and two-moment bulk microphysics schemes, with verification against polarimetric radar data. *Mon. Wea. Rev.*, **140**, 1457–1475, doi:10.1175/MWR-D-11-00032.1.

Kerr, C. A., D. J. Stensrud, and X. Wang, 2015: Assimilation of cloud-top temperature and radar observations of an idealized splitting supercell using an observing system simulation experiment. *Mon. Wea. Rev.*, **143**, 1018–1034, doi:10.1175/MWR-D-14-00146.1.

O'Dell, C. W., A. K. Heidinger, T. Greenwald, P. Bauer, and R. Bennartz, 2006: The successive-order-of-interaction radiative transfer model. Part II: Model performance and applications. *J. Appl. Meteor. Climatol.*, **45**, 1403–1413, doi:10.1175/JAM2409.1.

Okamoto, K., A. P. McNally, and W. Bell, 2014: Progress towards the assimilation of all-sky infrared radiances: An evaluation of cloud effects. *Quart. J. Roy. Meteor. Soc.*, **140**, 1603–1614, doi:10.1002/qj.2242.

Otkin, J. A., 2010: Clear and cloudy sky infrared brightness temperature assimilation using an ensemble Kalman filter. *J. Geophys. Res.*, **115**, D19207, doi:10.1029/2009JD013759.

——, 2012a: Assimilation of water vapor sensitive infrared brightness temperature observations during a high impact weather event. *J. Geophys. Res.*, **117**, D19203, doi:10.1029/2012JD017568.

——, 2012b: Assessing the impact of the covariance localization radius when assimilating infrared brightness temperature observations using an ensemble Kalman filter. *Mon. Wea. Rev.*, **140**, 543–561, doi:10.1175/MWR-D-11-00084.1.

Ott, E., and Coauthors, 2004: A local ensemble Kalman filter for atmospheric data assimilation. *Tellus*, **56A**, 415–428, doi:10.1111/j.1600-0870.2004.00076.x.

Parrish, D. F., and J. C. Derber, 1992: The National Meteorological Center's spectral statistical-interpolation analysis system. *Mon. Wea. Rev.*, **120**, 1747–1763, doi:10.1175/1520-0493(1992)120<1747:TNMCSS>2.0.CO;2.

Privé, N. C., Y. Xie, J. Woollen, S. E. Koch, R. Atlas, and R. Hood, 2013: Evaluation of the Earth Systems Research Laboratory's global Observing System Simulation Experiment system. *Tellus*, **65A**, 19011, doi:10.3402/tellusa.v65i0.19011.

Schenkman, A., M. Xue, A. Shapiro, K. Brewster, and J. Gao, 2011: The analysis and prediction of the 8–9 May 2007 Oklahoma tornadic mesoscale convective system by assimilating WSR-88D and CASA radar data using 3DVAR. *Mon. Wea. Rev.*, **139**, 224–246, doi:10.1175/2010MWR3336.1.

Schmit, T. J., M. M. Gunshor, W. P. Menzel, J. J. Gurka, J. Li, and A. S. Bachmeier, 2005: Introducing the next-generation Advanced Baseline Imager on GOES-R. *Bull. Amer. Meteor. Soc.*, **86**, 1079–1096, doi:10.1175/BAMS-86-8-1079.

Seemann, S. W., E. E. Borbas, R. O. Knuteson, G. R. Stephenson, and H.-L. Huang, 2008: Development of a global infrared land surface emissivity database for application to clear-sky sounding retrievals from multispectral satellite radiance measurements. *J. Appl. Meteor. Climatol.*, **47**, 108–123, doi:10.1175/2007JAMC1590.1.

Skamarock, W. C., and Coauthors, 2008: A description of the Advanced Research WRF version 3. NCAR Tech. Note NCAR/TN-475+STR, 113 pp., doi:10.5065/D68S4MVH.

Snyder, C., and F. Zhang, 2003: Assimilation of simulated Doppler radar observations with an ensemble Kalman filter. *Mon. Wea. Rev.*, **131**, 1663–1677, doi:10.1175//2555.1.

Stengel, M., 2008: Assimilation of SEVIRI's water vapour channel observations in clear-sky conditions into the HIRLAM model. HIRLAM Tech. Rep. 68, 54–64. [Available online at http://hirlam.org/index.php/component/docman/doc_view/163-hirlam-technical-report-no-68-paper-5-stengel?Itemid=71.]

——, P. Unden, M. Lindskog, P. Dahlgren, N. Gustafsson, and R. Bennartz, 2009: Assimilation of SEVIRI infrared radiances with HIRLAM 4D-Var. *Quart. J. Roy. Meteor. Soc.*, **135**, 2100–2109, doi:10.1002/qj.501.

——, M. Lindskog, P. Unden, and N. Gustafsson, 2013: The impact of cloud-affected IR radiances on forecast accuracy of a limited-area NWP model. *Quart. J. Roy. Meteor. Soc.*, **139**, 2081–2096, doi:10.1002/qj.2102.

Storm Prediction Center, 2015: Severe thunderstorm events. NOAA, accessed 1 February 2015. [Available online at http://www.spc.noaa.gov/exper/archive/event.php?date=20050604.]

Sun, J., and N. A. Crook, 1997: Dynamical and microphysical retrieval from Doppler radar observations using a cloud model and its adjoint. Part I: Model development and simulated data experiments. *J. Atmos. Sci.*, **54**, 1642–1661, doi:10.1175/1520-0469(1997)054<1642:DAMRFD>2.0.CO;2.

——, and ——, 1998: Dynamical and microphysical retrieval from Doppler radar observations using a cloud model and its adjoint. Part II: Retrieval experiments of an observed Florida convective storm. *J. Atmos. Sci.*, **55**, 835–852, doi:10.1175/1520-0469(1998)055<0835:DAMRFD>2.0.CO;2.

——, and ——, 2001: Real-time low-level wind and temperature analysis using single WSR-88D data. *Wea. Forecasting*, **16**, 117–132, doi:10.1175/1520-0434(2001)016<0117:RTLLWA>2.0.CO;2.

Thompson, G., R. M. Rasmussen, and K. Manning, 2004: Explicit forecasts of winter precipitation using an improved bulk microphysics scheme. Part I: Description and sensitivity analysis. *Mon. Wea. Rev.*, **132**, 519–542, doi:10.1175/1520-0493(2004)132<0519:EFOWPU>2.0.CO;2.

——, P. R. Field, R. M. Rasmussen, and W. R. Hall, 2008: Explicit forecasts of winter precipitation using an improved bulk microphysics scheme. Part II: Implementation of a new snow parameterization. *Mon. Wea. Rev.*, **136**, 5095–5115, doi:10.1175/2008MWR2387.1.

Tong, M., and M. Xue, 2005: Ensemble Kalman filter assimilation of Doppler radar data with a compressible nonhydrostatic model: OSS experiments. *Mon. Wea. Rev.*, **133**, 1789–1807, doi:10.1175/MWR2898.1.

Torn, R. D., G. J. Hakim, and C. Snyder, 2006: Boundary conditions for limited-area ensemble Kalman filters. *Mon. Wea. Rev.*, **134**, 2490–2502, doi:10.1175/MWR3187.1.

Vukicevic, T., T. Greenwald, M. Zupanski, D. Zupanski, T. Vonder Haar, and A. S. Jones, 2004: Mesoscale cloud state estimation from visible and infrared satellite radiances. *Mon. Wea. Rev.*, **132**, 3066–3077, doi:10.1175/MWR2837.1.

——, M. Sengupta, A. S. Jones, and T. Vonder Haar, 2006: Cloud-resolving satellite data assimilation: Information content of IR window observations and uncertainties in estimation. *J. Atmos. Sci.*, **63**, 901–919, doi:10.1175/JAS3639.1.

Wheatley, D. M., N. Yussouf, and D. J. Stensrud, 2014: Ensemble Kalman filter analyses and forecasts of a severe mesoscale convective system using different choices of microphysics schemes. *Mon. Wea. Rev.*, **142**, 3243–3263, doi:10.1175/MWR-D-13-00260.1.

——, K. Knopfmeier, T. A. Jones, and G. Creager, 2015: Storm-scale data assimilation and ensemble forecasting with the NSSL Experimental Warn-on-Forecast System. Part I: Radar data experiments. *Wea. Forecasting*, **30**, 1795–1817, doi:10.1175/WAF-D-15-0043.1.

Whitaker, J. S., and T. M. Hamill, 2002: Ensemble data assimilation without perturbed observations. *Mon. Wea. Rev.*, **130**, 1913–1924, doi:10.1175/1520-0493(2002)130<1913:EDAWPO>2.0.CO;2.

Xiao, Q., Y.-H. Kuo, J. Sun, W.-C. Lee, E. Lim, Y.-R. Guo, and D. M. Barker, 2005: Assimilation of Doppler radar observations with a regional 3DVAR System: Impact of Doppler velocities on forecasts of a heavy rainfall case. *J. Appl. Meteor.*, **44**, 768–788, doi:10.1175/JAM2248.1.

Yussouf, N., E. R. Mansell, L. J. Wicker, D. M. Wheatley, and D. J. Stensrud, 2013: The ensemble Kalman filter analyses and forecasts of the 8 May 2003 Oklahoma City tornadic supercell storm using single- and double-moment microphysics schemes. *Mon. Wea. Rev.*, **141**, 3388–3412, doi:10.1175/MWR-D-12-00237.1.

Zupanski, D., M. Zupanski, L. D. Grasso, R. Brummer, I. Jankov, D. Lindsey, M. Sengupta, and M. Demaria, 2011: Assimilating synthetic GOES-R radiances in cloudy conditions using an ensemble-based method. *Int. J. Remote Sens.*, **32**, 9637–9659, doi:10.1080/01431161.2011.572094.